Copper coverage effect on tungsten crystallites texture development in W/Cu nanocomposite thin films

Baptiste Girault, Dominique Eyidi, Thierry Chauveau, David Babonneau, Pierre-Olivier Renault, Éric Le Bourhis, Philippe Goudeau

Copper coverage effect on tungsten crystallites texture development in W/Cu nanocomposite thin films

B. Girault,[1,2,a)] D. Eyidi,[2] T. Chauveau,[3] D. Babonneau,[2] P.-O. Renault,[2] E. Le Bourhis,[2] and P. Goudeau[2]

[1]*INM–Leibniz Institute for New Materials, Campus Building D2 2, 66123 Saarbrücken, Germany*
[2]*Institut P', UPR 3346 CNRS, University of Poitiers, ENSMA, SP2MI, Bd Marie et Pierre Curie, BP30179, 86962 Futuroscope Cedex, France,*
[3]*LPMTM, UPR 9001 CNRS, Institut Galilée, University of Paris 13, 99 Avenue Jean-Baptiste Clément, 93430 Villetaneuse, France,*

Morphological and crystallographic structures of multilayered W/Cu nanocomposite thin films elaborated by physical vapor deposition were studied by varying copper and tungsten thicknesses. Sample examinations were performed by x-ray diffraction (XRD), grazing incidence small-angle x-ray scattering and transmission electron microscopy (TEM). Samples were found to be composed of copper nanoparticles, homogeneously dispersed in planes parallel to the film-substrate interface and periodically separated by tungsten layers along the growth direction. Our observations revealed an original texture development of the tungsten matrix from a mixture of unexpected α-W$\langle 111\rangle$ and α-W$\langle 110\rangle$ components to unique α-W$\langle 110\rangle$ component as the copper coverage passes a thickness threshold of 0.6 nm. Local TEM texture stereology investigations revealed simultaneous columnar growth of both preferential orientations posterior to polycrystalline development while XRD reveals strong compressive residual stresses in both texture components. Physical origins of the preferential crystallographic orientation evolution are discussed. Copper mono layers adsorption on W surfaces promotes surface energy anisotropy and diminution which is effective over the threshold. Below, the presence of a W(Cu) solid solution which does not affect substantially the texture is revealed by the stress-free lattice parameter value extracted from XRD.

I. INTRODUCTION

Composite materials comprise all close associations between immiscible materials resulting in a material presenting different properties as compared to the original elements taken separately. In most cases, composites can be described as one or several materials randomly dispersed or organized in a binding media that is called the matrix. Physical properties of solid materials are strongly linked to their microstructure. Modification of one or several microstructural parameters such as the chemical composition, the atomic layout or dimensions leads to properties evolution.[1] As a result, synthesis of materials endowed with novel properties, controlling their microstructure from the atomic to macroscopic scales, is an important field in material science, chemistry or biology. Nanomaterials encompass all materials presenting at least one nanometer length scale leading to a high grain boundaries density.[2,3] Their mechanical properties may differ significantly from their bulk counterparts.[4–10] The processes responsible for these changes are not fully understood yet and are believed to be caused by an increase in grain-surface and grain-boundary volumes, which become dominant over the bulk at the nanoscale. Changes are further caused by boundary conditions at the free surface and at the interface with the substrate which become non negligible for thin films.[11,12] To get further insight into those complex phenomena, tailored and model structures are demanded.

Tungsten–copper composites are promising materials for microelectronic applications. The combination of the high thermal conductivity of copper and the low thermal expansion coefficient of tungsten renders W–Cu composites attractive for thermal management applications such as heat sink for high density integrated circuits.[13,14] Their electrical properties also make them promising materials for high voltage contacts.[15–17] Applications of these metallic matrix composites are numerous since they present interesting mechanical strength resulting from the compromise between the high strength of W and the ductility of Cu while size effects are expected for multilayer coatings (e.g., in the international thermonuclear experimental reactor).[18,19] W–Cu composites are thus strongly studied for harsh conditions.[20–22]

Literature offers a large spectrum of processes that allow elaborating W–Cu composites.[23] Most commonly used methods are those involving liquid phase sintering by infiltration,[15] activated sintering,[24] powder melt,[25] and other slow, expensive and complex processes[26–30] like chemical synthesis for example. Factors that can affect their electrical and thermal conductivity are the composition, porosity, impurity level and grain size.[17,31] However, full densification of tungsten–copper composites remains difficult because of the poor solubility at thermodynamic equilibrium (high positive melting enthalpy value, $\Delta H = +35.5$ kJ/mol for equiatomic composition).[32]

[a)]Electronic mail: baptiste.girault@inm-gmbh.de.

One way to circumvent this difficulty is to deposit the material using physical vapor deposition (PVD) methods. Out of equilibrium states may be reached due to mixing effects resulting from ion implantation during thin-film growth[33] under energetic deposition process[34] and also to anomalous interfacial diffusion resulting from size-dependent diffusion coefficients.[35–37] Also, with PVD methods, the structure can be tailored using sequenced deposition.

The control of the nanostructure of W/Cu coatings requires a full understanding of the growth mechanisms of both Cu and W phases. Grain size and texture have to be characterized at different scales while residual stresses have to be analyzed in view of the structure and deposition conditions.[38]

X-ray diffraction (XRD) is one of the most commonly used techniques to determine the structural characteristics of thin films (texture and grain size) and residual stress state in small crystalline volumes.[39,40] It is phase-selective and allows the determination of both the elastic properties and the microstructural state of the diffracting phases. Furthermore, small scale mechanical behavior of polycrystalline materials can be investigated thanks to *in situ* diffraction studies for which, model single phase and single textured components are demanded.[41] However, the extracted information is averaged over the illuminated volume. Complementary measurements are then necessary to obtain local structural information. In particular, transmission electron microscopy (TEM) observations on cross-sectional samples are of paramount importance to provide structural information at a subnanometer length scale.

The present paper reports a study on tungsten sublayer microstructure and texture evolution in stratified W/Cu composite systems (multilayer type) obtained by PVD when changing both tungsten sublayer thickness and copper interlayer thickness.

II. EXPERIMENTAL TECHNIQUES

A. Samples elaboration

The stratified W/Cu thin films were deposited at room temperature by ion beam sputtering with a focused Ar^+ ion-gun at 1.2 keV (multicusp radio-frequency source) in a NORDIKO-3000 system. During film growth, the ion-gun was supplied with a constant incident radio-frequency power (165 W) and constant Ar flux of 10 standard cubic centimeter per minute. The 150 mm diameter targets were sputtered during 10 min allowing both ion-gun stabilization and target pollution cleaning caused by vacuum break. Gas pressure in the ion-gun was estimated to vary between 0.1 and 1 Pa. The ion-gun axis was inclined at 45° to the normal of the surface target while the sample surface was parallel to the target plane. An elliptical diaphragm at the ion-gun exit allowed getting a circular sputtered surface of 80 mm in diameter on the target to ensure a good purity of sputtered atoms. These characteristics lead to deposited atom energy distribution centered around 5 eV with a non-negligible tail (10% contribution) between 5 and 100 eV. Thin-film deposition was performed in a no load-locked sputtering chamber equipped with two cryogenic pumps. Hence, the sputtering chamber was pumped down to a base pressure of 2×10^{-6} Pa. At the working pressure during film growth ($\sim10^{-2}$ Pa), the mean free path was determined to be longer than the target-substrate distance, leading to nonthermalized incident atoms with high residual stresses built in the deposited thin films.

Two types of substrates were used: 200 and 650 μm thick naturally oxidized Si(001) wafers. They were preliminary cleaned with acetone and ethanol and finally dried with an argon gas jet prior to their introduction in the deposition chamber. The rotating sample holder of 120 mm in diameter allowed introducing all the substrates in a single run. Tungsten and copper growing rates were previously calibrated by x-ray reflectometry (XRR) and were found to be 0.05 nm s^{-1} and 0.16 nm s^{-1}, respectively.

One stratified sample series was prepared with a constant 3 nm nominal tungsten sublayer thickness and copper interlayer thicknesses ranging from 1 down to zero nm (per period). Samples with no copper between tungsten layers were produced to test sequenced tungsten deposition considering a holding time of 51 s between the depositions of two successive W layers. Two additional samples with 0.5 nm nominal copper interlayer thickness and tungsten sublayer thicknesses of 1.5 and 12 nm, were also prepared. In the following, the samples are labeled W/Cu x/y with x and y referring to W and Cu thicknesses, respectively.

B. Characterization methods

XRD measurements were carried out on a four-circle SEIFERT XRD 3000 diffractometer (Cu K_α radiation, $\lambda_{Cu\,K\alpha}$=0.15406 nm) with a point focus beam to quantify films texture and residual stresses, and with a line focus beam to characterize thin-film stratification.

1. Sample geometry

XRR was systematically performed in order to evaluate sample stratification using the Bragg law at a grazing incidence angle.

Energy-dispersive x-ray spectroscopy was used in a scanning electron microscope to determine the atomic concentrations of copper and tungsten in the films and to estimate the effective tungsten and copper sublayers thicknesses (per period) employing the period Λ obtained by XRR

$$\frac{t_{Cu}}{t_W} = \frac{\text{at. \% Cu}}{\text{at. \% W}} \times \frac{M_{Cu}}{M_W} \times \frac{\rho_W}{\rho_{Cu}}, \tag{1}$$

with $t_W+t_{Cu}=\Lambda$ and where t, ρ, M, and at. % stand for the thickness, density, atomic mass, and atomic proportion, respectively.

Since copper sublayers contain only a few atomic layers, the possible formation of Cu dispersoids within a W matrix was investigated by grazing incidence small-angle x-ray scattering (GISAXS) measurements performed at European Synchrotron Radiation Facility on the CRG-BM02 beamline. GISAXS is sensitive to the size, shape, and organization of heterogeneities in the electron density distribution in the nanometer-range. The used x-ray wavelength was 0.177 nm (7 keV) while the incident angle was 0.8° just above the bulk W critical angle for total reflection (0.64° for 7 keV). The

beam size was 500 μm horizontally and 100 μm vertically. GISAXS patterns were recorded with a Princeton two-dimensional (2D) detector and the acquisition time varied between 30 and 60 min depending on the sample signal. The experimental data were analyzed with the FITGISAXS package developed within the IGOR PRO analysis software (WaveMetrics, Inc.).[42]

2. Phase analysis

Tungsten crystallizes into two different phases: the equilibrium pure phase, so-called α-W or tungsten Wolfram which is body-centered-cubic (bcc structure with $Im\bar{3}m$ space group) and a second one that is a low oxidized tungsten phase, called W_3O-A15 or β-W (Refs. 43–45) with A15 structure (space group $Pm\bar{3}n$). Systematic qualitative phase analyses were performed on each sample with an INEL XRG 3000 x-ray diffractometer equipped with a linear detector (CPS 120) using Cr K_α radiation ($\lambda_{Cr\,K\alpha}$=0.228 97 nm) in an asymmetric $\Omega/2\theta$ geometry (Ω=30°).

3. Texture analysis

Pole figures were systematically determined on α-W{110}, α-W{200}, and α-W{211} tungsten diffraction peaks in order to get crystallographic orientation distribution function (CODF). Pole figures were performed with ψ angles (angle between the normal to the sample surface and the normal to the diffracting planes) ranging from 1.25° to 78.75° with a 2.5° step and φ angles (rotational angle around the normal to the sample surface) ranging from 0° to 360° with a 5° step. The integration time was 6 s per point. Background pole figures were systematically recorded for each of them. They were completed on diffraction peak bottom (2θ) with a 3 s counting time. CODF were determined with the LABOTEX software[46] which crystallographic orientation analysis is based on the arbitrary defined cells method[47] that essentially uses the WIMV algorithm.[48–50] This allows proper discrimination of polycrystalline components from possible reinforcements due to minor texture components. Texture component volume fractions were calculated after entering disorientation conditions of 10° in both φ and φ_2 Euler's angles around the main fiber texture components (α-W$\langle 110\rangle$ and α-W$\langle 111\rangle$), and of 2.5° in φ and 7.5° in φ_2 for representative secondary texture components α-W$\langle 221\rangle$ and α-W$\langle 331\rangle$ (orientation reinforcements), with regards to other components proximity.

4. Stress determination

High-angle XRD measurements were performed on each sample to evaluate intragranular macroscopic residual stresses in the tungsten sublayers. The low copper quantities deposited prevent any signal from the copper interlayers to be measured. The so-called "$\sin^2\psi$ method" based on the variation in the diffraction peak position with $\sin^2\psi$ was used.[39,40] This method is particularly suitable in the case of a locally isotropic material like tungsten. Moreover, the deposition geometry allows assuming an equibiaxial stress state and, thus the "$\sin^2\psi$ relation" can be written as

$$\varepsilon_{\varphi\psi} = \frac{1+\upsilon}{E}\sigma_r \sin^2\psi - \frac{2\upsilon}{E}\sigma_r, \tag{2}$$

where $\varepsilon_{\varphi\psi}$ is the strain in the direction (φ,ψ), σ_r is the equibiaxial residual stress, and E and ν are the Young's modulus and the Poisson's ratio of the studied material, respectively.

Here, the rational definition of strain $\varepsilon_{\varphi\psi}=\ln(a_{hkl}/a_0)$ is used, a_0 being the stress-free lattice parameter and a_{hkl} the measured lattice parameter.[40,51] As a first approximation, the tungsten bulk elastic constants (E=411 GPa and ν=0.28) were used.[51] The considered tungsten diffraction peaks for this analysis have been measured around pole directions.

Thin-film macroscopic residual stresses were determined using the curvature method. Curvatures before and after deposition were measured using a Dektak® IIa profilometer on 200 μm thick Si cantilever substrates.[51] Since the substrate is much thicker than the deposited thin film and considering that the strain is continuous at the film-substrate interface, the Stoney's relationship can be applied

$$\sigma_r^f = \frac{E_s}{1-\upsilon_s} \times \frac{t_s^2}{6t_f}\left(\frac{1}{R_{final}} - \frac{1}{R_{initial}}\right), \tag{3}$$

with $(E_s/1-\upsilon_s)$=180.5 GPa for Si (001) wafers. σ_r^f is the macroscopic stress set in the film, E_s and υ_s are the substrate Young's modulus and Poisson's ratio, respectively, t_s and t_f are the substrate and film thicknesses, and lastly, $R_{initial}$ and R_{final} are the curvature radii before and after deposition. Noticeably, this method does not require the knowledge of thin-film elastic constants and yields the average stress in the thin film.

Combining both curvature method and x-ray residual stress analysis allows evaluating the global contribution of the copper interlayers, interfaces, and grain boundaries. Indeed, XRD yields information on the crystalline W fraction while the curvature method assesses the whole thin-film response.

5. Microstructural investigations

Bright-field (BF) TEM experiments were carried out on a W/Cu 12/0.5 sample which exhibits the largest tungsten thickness. Cross-sectional specimens were prepared as follows: two pieces $2.7\times1.5\times0.65$ mm^3 in size were cut from a 650 μm thick Si-coated substrate with a wire saw. They were then bond in pairs, the film surfaces stuck to each other by M-Bond glue. The TEM sample was first ground using P 320 silicon carbide disk down to a thickness of 200 μm. Mirror polish was obtained on both surfaces using 1200 to 4000 silicon carbide disk. Samples were then set in a dimple grinder (DG, Gatan model 656) to produce a 20 μm thick dimpled surface. Finally, the sample was ion-milled to electron transparency with a precision ion polishing system (Gatan model 691). TEM observations were performed on a JEOL 2200-FS equipped with a field-emission gun at an acceleration voltage of 200 kV.

Dark-field (DF) TEM was performed with the selected area electron diffraction mode to localize textured areas by choosing diffraction spots aligned along the growth direc-

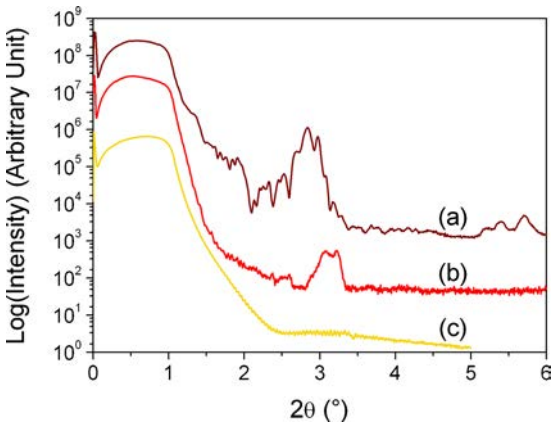

FIG. 1. (Color online) XRR curves obtained on (a) W/Cu 3/1, (b) W/Cu 3/0.5, and (c) W/Cu 3/0. For sake of clarity, a logarithmic scale is used for intensities.

tion. Superposition of DF-TEM images allowed qualitative stereometry of crystallographic orientations in the observation plane since DF-TEM image intensities are related to the selected orientation and structure factors of the chosen spots.

For a further understanding of crystallographic orientation development, electron nanobeam diffraction patterns were acquired from film-substrate interface to surface at several locations. This technique was carried out with a 0.5 nm probe size (full width at half maximum, FWHM) and allowed local investigations on areas of ~ 2 nm in size.[52]

III. RESULTS

A. Sample stratification

Figure 1 presents XRR curves from W/Cu 3/1, W/Cu 3/0.5, and W/Cu 3/0. All samples present small angle Bragg's peaks shifting to larger angle values as the copper sublayer thickness (thus period) decreases. Amazingly, despite the signal weakness, stratification is also detected with sequenced tungsten deposited layers (W/Cu 3/0). It reveals the existence of a pseudo "interfacial layer" or at least a periodical electron density modulation along the film growth direction. This modulation could be the result of surface reconstruction or impurities incorporation during sequenced tungsten deposition holding time. However, the integral intensity of the first order small angle Bragg's peak is decreasing while decreasing the copper thickness, revealing a loss of stratification quality related to the copper coverage rate decrease evidenced below. Results deduced from these XRR curves are shown in Table I.

Even if the stratification of the 1 nm nominal copper interlayer thickness sample is the only one that allows detecting the second order of Bragg's reflection, the shape of the Bragg's peak suggests important interface irregularities between the tungsten and copper sublayers. GISAXS measurements were carried out on both W/Cu x/0.5 and W/Cu x/1 (x=1.5, 3, and 12) specimens to evaluate copper layers continuity. As typical examples, Figs. 2(a) and 2(b) show the 2D GISAXS patterns of W/Cu 12/1 and W/Cu 12/0.5, which exhibit diffuse spots symmetrically located on either sides of the q_z axis. These results prove copper sublayer discontinuity,[53] i.e., copper sublayers of W/Cu x/1 and W/Cu x/0.5 formed by isolated copper nanoparticles. Quantitative analysis of the GISAXS data was performed from horizontal cuts obtained at $q_z = 1.2$ nm^{-1} [symbols in Fig. 2(c)], by assuming that the scattered intensity originated from spheroidal particles homogeneously dispersed in planes parallel to the film-substrate interface with no vertical correlation between particles (i.e., each Cu layer has a morphology which is completely independent from the adjacent Cu layers).[53] The best fits to the experimental data [solid lines in Fig. 2(c)] yield an average in-plane particle diameter $D_p = 3.9$ nm and an interparticle distance $L_p = 8.7$ nm for W/Cu 12/1, while $D_p = 3.0$ nm and $L_p = 8.3$ nm were found for W/Cu 12/0.5. The evolution of these values indicates a coalescence regime correlated with an increase in the coverage rate T of tungsten surface with copper islands which can be calculated thanks to the in-plane information extracted from GISAXS signal. The coverage rate formula is given by

TABLE I. Morphology, structure, and mechanical state for the samples W/Cu 3/1, W/Cu 3/0.5, W/Cu 3/0, W/Cu 12/0.5, and W/Cu 1.5/0.5: Λ, t_i, and σ_i^r correspond to period, thickness, and residual stress, respectively, associated to subscript i (W, Cu, or f). W or Cu refers, respectively, to tungsten or copper sublayer and f to the film. Global residual stresses in the film were obtained by substrate curvature. Residual stresses in tungsten sublayer were determined by XRD measurements; pole direction discrimination allowed to determine residual stresses associated to α-W⟨110⟩ and α-W⟨111⟩ oriented grains. $\langle\sigma_r^W\rangle$ corresponds to the residual stress obtained combining data from α-W⟨110⟩ and α-W⟨111⟩ pole directions. a_0^W is the tungsten stress-free lattice parameter associated to main texture components. Experimental uncertainties on stresses and effective thicknesses are about 10%.

	Effective thicknesses (nm)				Residual stresses (GPa)			Stress-free lattice parameter a_0^W (nm)	W grain texture component
W/Cu	Λ	t_W	t_{Cu}	t_f	σ_r^f	$\langle\sigma_r^W\rangle$	σ_r^W		
3/1.0	3.3	2.7	0.6	205	−1.5	−3.5	−3.5	0.3185 ± 0.0003	⟨110⟩
3/0.5	3.0	2.8	0.2	198	−3.2	−5.8	−5.6	0.3171 ± 0.0003	⟨110⟩
							−6.4	0.3173 ± 0.0003	⟨111⟩
3/0.0	3.1	3.1	0	217	−2.7	−4.7	−3.4	0.3182 ± 0.0003	⟨110⟩
							−5.7	0.3189 ± 0.0003	⟨111⟩
12/0.5	11.0	10.8	0.2	174	−2.8	−5.3	−5.0	0.3175 ± 0.0003	⟨110⟩
							−5.5	0.3176 ± 0.0003	⟨111⟩
1.5/0.5	1.7	1.5	0.2	185	−3.2	−6.8	−8.1	0.3144 ± 0.0003	⟨110⟩
							−3.3	0.3134 ± 0.0003	⟨111⟩

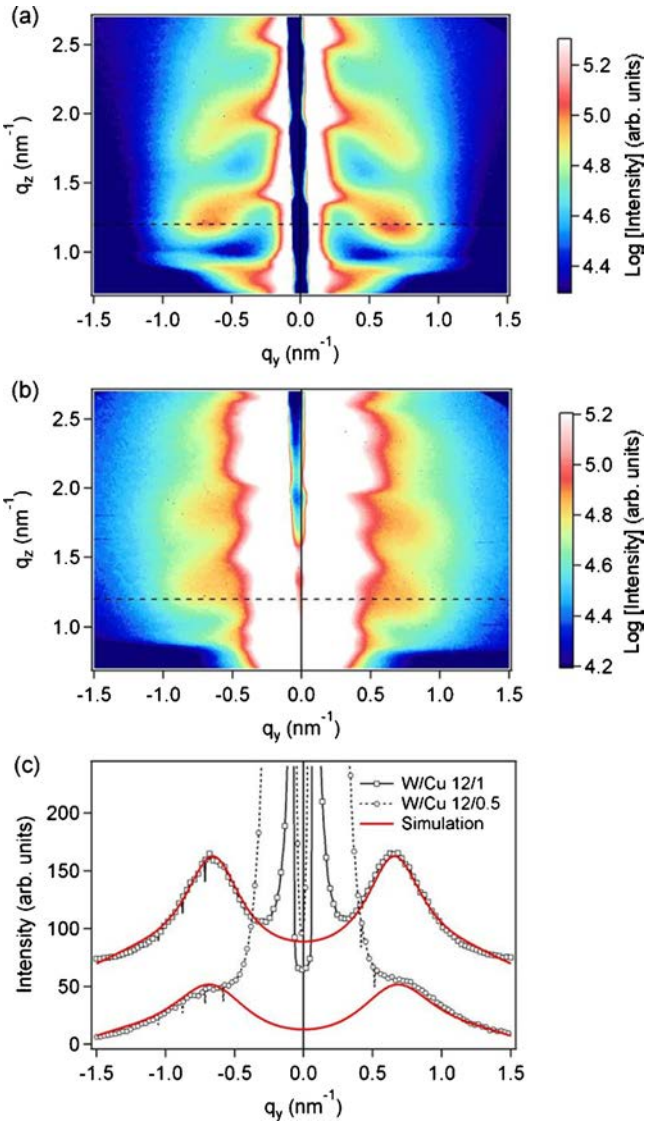

FIG. 2. (Color online) 2D GISAXS patterns obtained on (a) W/Cu 12/1 and (b) W/Cu 12/0.5. (c) Measured (symbols) and fitted (solid lines) horizontal cuts collected along the dotted lines in (a) and (b). The data of the W/Cu 12/1 sample have been shifted upward for clarity.

$$T = \pi D_p^2 / L_p^2. \quad (4)$$

We found $T \sim 0.41$ and 0.63 for 0.2 nm and 0.6 nm Cu thicknesses, respectively. The coverage rate value significantly increases by about 40% whereas the average copper thickness is multiplied by 3 (200%). However, as discussed below, the threshold for having single texture is reached.

B. Phase analysis

Figure 3 shows $\Omega/2\theta$ diffractograms carried out on the W/Cu 3/1, W/Cu 3/0.5, and W/Cu 3/0 samples. On the one hand, no signal from copper was detected because of the small diffracting volumes. On the other hand, phase analysis revealed that deposited tungsten mainly crystallized in α-W (bcc) although a small fraction of β-W was detected on the tungsten sequenced deposition sample (W/Cu 3/0). Almost no evolution of the FWHM of the α-W{110} diffraction peak was observed when the copper sublayer thickness was decreased. Neglecting the microstrains, this observation reveals that the tungsten grain size remains unchanged.

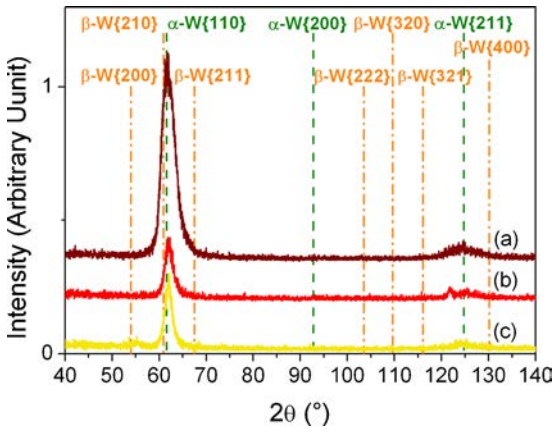

FIG. 3. (Color online) $\Omega/2\theta$ diffractograms obtained on the samples (a) W/Cu 3/1, (b) W/Cu 3/0.5, and (c) W/Cu 3/0 (Ω=30°). Dotted vertical lines represent bulk diffraction peak position of the α- and β-tungsten phases [International Center for Diffraction Data—Powder Diffraction File No. 4–806 (α-W) and No. 47-1319 (β-W)].

C. Crystallographic texture

Pole figures obtained on α-W{110} diffraction peak for W/Cu 3/1, W/Cu 3/0.5, and W/Cu 3/0 are shown in Fig. 4.

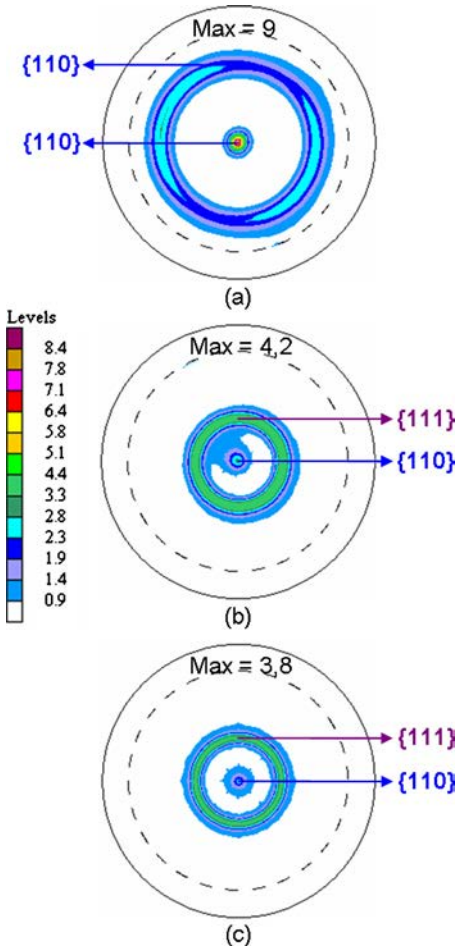

FIG. 4. (Color online) Pole figures obtained on α-W{110} diffracting planes of (a) W/Cu 3/1, (b) W/Cu 3/0.5, and (c) W/Cu 3/0.

TABLE II. Volume fractions of the different fiber texture components for the samples W/Cu 3/1, W/Cu 3/0.5, and W/Cu 3/0. α-W$\langle 331\rangle$ and α-W$\langle 221\rangle$ fiber texture components reflect crystallographic orientation distribution between the two main fiber texture components α-W$\langle 110\rangle$ and α-W$\langle 111\rangle$. Isotropic contribution refers to random or polycrystalline component and is very sensitive to the background. The relative uncertainties are about 10%. Increase in tungsten interlayer (Cu) thickness leads to the loss of the α-W$\langle 111\rangle$ preferential crystallographic orientation. For a constant 0.5 nm copper nominal thickness, the ratio between main texture components volume fraction is nearly constant with growing tungsten thickness whereas isotropic and distributed components (α-W$\langle 331\rangle$ and α-W$\langle 221\rangle$) volume fractions are decreasing.

	Volume fraction (%)				
W/Cu	α-W$\langle 111\rangle$	α-W$\langle 110\rangle$	α-W$\langle 331\rangle$	α-W$\langle 221\rangle$	Isotropic
3/1.0	1.5	51	2	5.5	40
3/0.5	43	12	6	2	37
3/0.0	27.5	9	3	3.5	57
12/0.5	38	12	8	2	40
1.5/0.5	22	6	9	11	52

Central peaks (ψ=0°) indicate systematically a population of α-W$\langle 110\rangle$ grains oriented along the growth direction. Radial intensity reinforcements reveal favored grain growth along crystallographic orientations, isotropically distributed in the plane (fiber texture). The pole figure of W/Cu 3/1 exhibits a high intensity ring located at ψ=60°, which corresponds to the angle between (110) and (011) planes in cubic crystals. Hence, this intense ring is related to the preferential orientation observed at ψ=0° and attests a $\langle 110\rangle$ fiber textured of the tungsten sublayers.

In contrast, rings observed on W/Cu 3/0.5 and W/Cu 3/0 pole figures indicate α-W{110} planes at about 35° from the sample surface. This value nearly matches the 35.3° angle existing between α-W$\langle 110\rangle$ and α-W$\langle 111\rangle$ directions for a bcc crystal and indicates thus a second α-W$\langle 111\rangle$ fiber texture component. Moreover, no ring is observed at ψ=60° suggesting a larger α-W$\langle 111\rangle$ volume fraction than the α-W$\langle 110\rangle$ one. This analysis is confirmed by measurements of α-W{200} and α-W{211} pole figures. Tungsten sublayers in W/Cu 3/0.5 and W/Cu 3/0 mainly consist of two sets of grains showing α-W$\langle 110\rangle$ and α-W$\langle 111\rangle$ fiber texture components. Pole figure investigations reveal bimodal crystallographic orientation development in tungsten sublayers below a copper sublayer thickness threshold of 0.6 nm (inter-tungsten sublayer).

Full texture analyses, carried out on all samples from α-W{110}, α-W{200}, and α-W{211} pole figures, lead to texture component volume fractions shown in Table II. W/Cu 3/1, W/Cu 3/0.5, and W/Cu 3/0 inverse pole figures are presented in Fig. 5 and are consistent with pole figure angular analysis. Inverse pole figures (a) and (b) of Fig. 5 also show a crystallographic reinforcement spread between the two main fiber texture components α-W$\langle 110\rangle$ and α-W$\langle 111\rangle$. These additional fiber texture components were taken into account considering two secondary components representative of this crystallographic reinforcement, i.e., α-W$\langle 331\rangle$ and α-W$\langle 221\rangle$ in quantitative volume fraction analysis. All

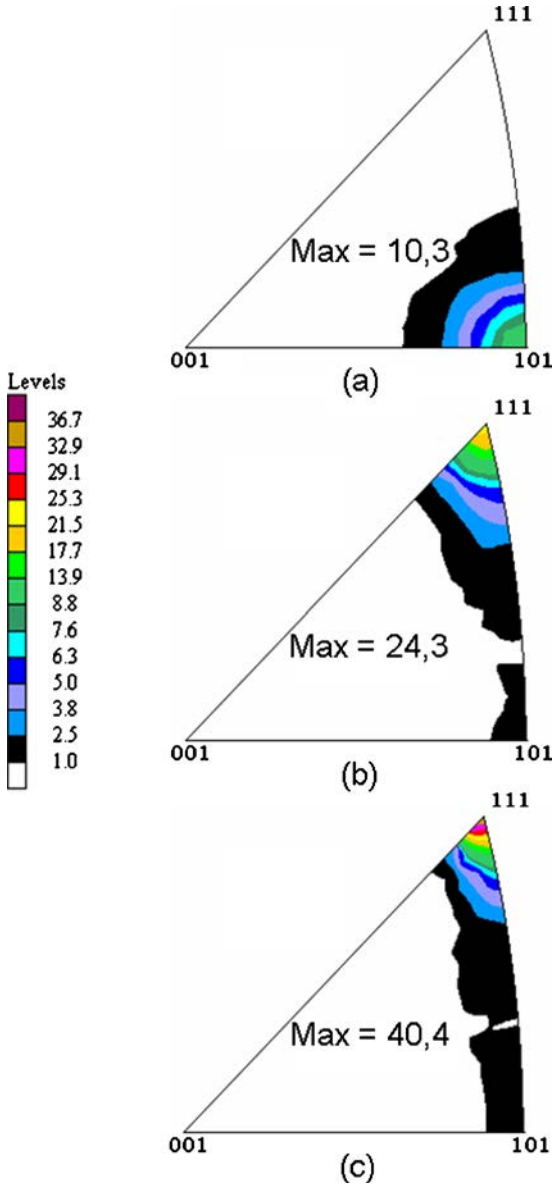

FIG. 5. (Color online) Inverse pole figures of (a) W/Cu 3/1, (b) W/Cu 3/0.5, and (c) W/Cu 3/0 (corrected from background, absorption, and defocusing).

samples display large isotropic proportion including polycrystalline component and most of these show bimodal α-W$\langle 110\rangle$ and α-W$\langle 111\rangle$ preferential orientations except W/Cu 3/1 which presents only α-W$\langle 110\rangle$ fiber texture.

Then, considering the sample series of 3 nm tungsten nominal thickness, texture evolution can be related to interlayer changes. It reveals that volume fraction ratio between α-W$\langle 111\rangle$ and α-W$\langle 110\rangle$ fiber texture components decreases from 7.5 down to 0 as the copper sublayer thickness rises from 0 up to 0.6 nm. Increasing the amount of copper leads to the dramatic loss of α-W$\langle 111\rangle$ preferential crystallographic orientation at 0.6 nm copper thickness.

Moreover, considering the sample series with 0.5 nm copper nominal thickness, texture evolution can be related to tungsten layer thickness. The volume fraction of α-W$\langle 111\rangle$ fiber texture component remains unchanged (constant volume fraction ratio of 3.5 between α-W$\langle 111\rangle$ and α-W$\langle 110\rangle$ preferential orientations). Furthermore, CODF evolution is

characterized by a progressive reinforcement of the α-W$\langle 111\rangle$ fiber texture component mainly at the expense of the polycrystalline volume fraction. It can be concluded that tungsten first growing stages are characterized by a strong polycrystalline component followed by the development of two major preferential crystallographic orientations. These favored crystallographic orientations reach an asymptotic volume of about two thirds of the crystal volume whereas their volume fraction ratio remains unchanged.

D. Stress analysis

Results obtained from residual stress analysis are shown in Table I which includes values for both stress-measurement methods used for thin films: curvature method and XRD analysis. Latter technique allowed determining not only the averaged tungsten crystallites residual stress and stress-free lattice parameter but also those associated to each of the major preferential orientations (α-W$\langle 110\rangle$ and α-W$\langle 111\rangle$ oriented grain families). This was performed discriminating pole directions with respect to texture components, using identical intrinsic mechanical properties for both crystallographic orientations since W is elastically isotropic.

As observed in Table I, all thin films and tungsten sublayers are under strong compressive stress state. Both α-W$\langle 110\rangle$ and α-W$\langle 111\rangle$ oriented grain families also present a strong compressive stress state. Stress analyses reveal systematically higher residual stresses in α-W$\langle 111\rangle$ oriented grains than in α-W$\langle 110\rangle$ ones.

The residual stress difference between these two crystallite families tends to decrease as the copper sublayer thickness increases. This is highlighted in Fig. 6 which shows logarithmic plots of measured lattice parameters as a function of $\sin^2\psi$ for W/Cu 3/1, W/Cu 3/0.5, and W/Cu 3/0.

Most determined stress-free lattice parameter values are larger than the bulk reference parameter (0.3165 nm), indicating lattice expansion due to interstitial defects.[54] This parameter reaches the highest values (~0.3185 nm) for 0.6 nm copper thickness (threshold for obtaining a single $\langle 110\rangle$ texture component) and without copper interlayer. For 0.2 nm copper thickness, the stress-free parameter reaches its lowest value (~0.3175 nm). This could imply copper diffusion into the α-W lattice. This effect is stronger when the W thickness is decreased as shown in Table I. In that case, this may reveal a large proportion of copper atoms substituted in the tungsten lattice. Copper abnormal diffusion has been previously observed for equinanometric thickness W/Cu multilayers.[35,37] Furthermore, energetic incident particle implantation during thin-film growth could also be involved in the solid-solution formation W(Cu). The copper content inside tungsten sublayers can be estimated using a simple model developed for diluted solid solutions[55]

$$\frac{\Delta V}{V} = 3\frac{\Delta a}{a} = 3f\frac{\gamma^W}{\gamma^{Cu}}P, \tag{5}$$

where $\Delta V/V$ is the tungsten relative volume variation, P is the atomic proportion of copper in substitution. γ^W and γ^{Cu} are the Eshelby factors for tungsten and copper, respectively, and f is a size factor.

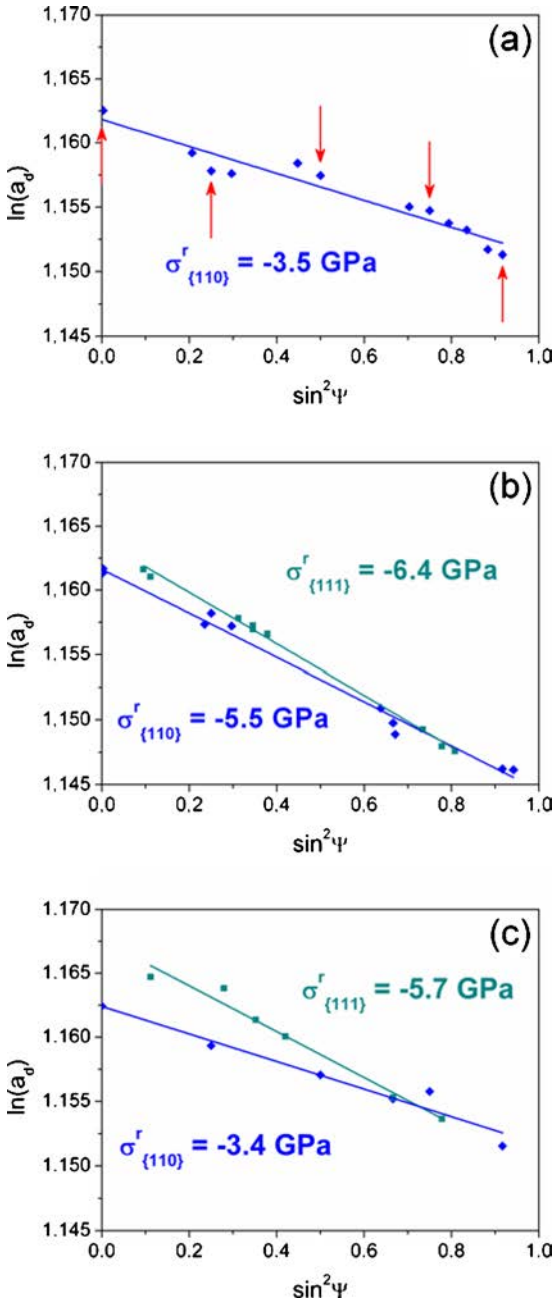

FIG. 6. (Color online) Logarithmic plots of deformed lattice parameter extracted from XRD measurements done on (a) W/Cu 3/1, (b) W/Cu 3/0.5, and (c) W/Cu 3/0 as a function of $\sin^2\psi$. XRD measurements were carried out around pole directions discriminating data associated to α-W$\langle 110\rangle$ and α-W$\langle 111\rangle$ fiber texture components when existing. Arrows indicate exact α-W$\langle 110\rangle$ pole directions data.

Eshelby and size factors are given by the following equations, with ν^i and r^i being the Poisson's ratio and equilibrium radius, respectively, subscript i being for either W or Cu

$$\gamma^i = 3\frac{1-\nu^i}{1+\nu^i}, \tag{6a}$$

$$f = \frac{r^{Cu} - r^W}{r^W}. \tag{6b}$$

Taking r^W=0.139 nm, r^{Cu}=0.128 nm, ν^W=0.280, and ν^{Cu} =0.345, the atomic proportion of substituted copper is deter-

mined to be approximately 7.3 at. % for α-W$\langle 110\rangle$ oriented grains in W/Cu 1.5/0.5. This value is slightly lower than that found by Villain for W/Cu 1.5/1.5 (8.7 at. %).[51] We found a higher value (10.7 at. %) for α-W$\langle 111\rangle$ oriented grains. Noticeably, all these concentrations are relatively low and may not significantly influence the elastic properties. Atomistic simulations showed in the case of Li–Mg cubic alloys, that the compressibility modulus increases by about 8% for 10 at. % magnesium ($r^{Mg}=0.160$ nm) in lithium ($r^{Li}=0.152$ nm).[56] In high concentrated bcc solid solution (50%) with small atomic radii difference as in Mo($r^{Mo}=0.139$ nm)−Rh($r^{Rh}=0.137$ nm) and Fe($r^{Fe}=0.126$ nm)−Cr($r^{Cr}=0.128$ nm), instrumental and numerical studies showed weak effects.[57,58] The mechanical influence of tungsten interlayers (copper sublayer and/or interfaces) can be evaluated considering the difference between macroscopic and microscopic residual stresses. In fact, tensile stresses are expected in copper sublayer whereas its contribution to macroscopic thin-film residual stress remains weak because of the thickness ratio between copper and tungsten (7% and 19% of the film thickness for 0.2 nm and 0.6 nm copper sublayer thicknesses, respectively). The evolution of the crystallite stress difference can be correlated with the texture evolution, i.e., a unique α-W$\langle 110\rangle$ fiber texture component volume fraction when copper thickness reaches the threshold value of 0.6 nm (W/Cu 3/1).

E. Simultaneous formation of fiber texture components

In Fig. 7(a), the BF-TEM image of W/Cu 12/0.5 specimen shows a periodic contrast and confirms the sample stratification. The observed period (11.3 nm) is close to that measured by XRR (11.0 nm).

Figure 7(b) shows the superposition of two DF-TEM images corresponding to the α-W$\langle 110\rangle$ and α-W$\langle 111\rangle$ preferential orientations. They were obtained using the α-W{110} and α-W{222} electron diffraction spots along the growth direction. The α-W{222} spot was used since in bcc α-W the 111 reflection is forbidden. These DF-TEM analyses were made for the W/Cu 12/0.5 specimen in the zone visible in Fig. 7(a). Darken areas in Fig. 7(b) correspond to α-W$\langle 110\rangle$ and α-W$\langle 222\rangle$ orientations. Since the structure factors associated to α-W$\langle 110\rangle$ and α-W$\langle 222\rangle$ are different, only qualitative comparison can be performed between the two DF-TEM images. Indeed, with equal diffracting planes population, α-W{222} spot intensity is only 3.6% of the α-W$\langle 110\rangle$ one. This calculation is based on PRDW atomic form factor. However, it still allows relative positioning of the main fiber texture components (α-W$\langle 110\rangle$ and α-W$\langle 111\rangle$). Comparison between (a) and (b) in Fig. 7 shows no correlation between interface positions and preferential orientation development.

Similar analyses of α-W$\langle 110\rangle$ and α-W$\langle 111\rangle$ orientations performed at different locations showed similar results. Figure 8 shows the superposition of the DF-TEM images associated to α-W$\langle 110\rangle$ and α-W$\langle 111\rangle$ fiber texture components in two other zones of the W/Cu 12/0.5 specimen at lower magnification. Evidence is obtained that grains contributing to either α-W$\langle 110\rangle$ or α-W$\langle 111\rangle$ fiber texture components build simultaneously in a columnar structure whose width ranges between 20 and 50 nm. No component alternation is observed along the growth direction but rather in the film plane. Oriented zones are not observed in the immediate vicinity of the film-substrate interface. This intermediate layer extends on approximately 10 to 50 nm from the interface prior to α-W$\langle 110\rangle$ or α-W$\langle 111\rangle$ textured grains. Latter columns extend up to the film surface without any influence from the copper sublayer.

In order to understand the development of the fiber texture components, several electron nanobeam diffraction (named "nanodiffraction") patterns were acquired at various positions distributed from the film-substrate interface to the top surface of the film. The beam was focused on α-W$\langle 110\rangle$ and α-W$\langle 111\rangle$ oriented zones as well as along a zone presenting none of these two major fiber texture components. Nanodiffraction positions are shown in Fig. 7(c) which also shows typical nanodiffraction patterns obtained in related zones. Analysis of nanodiffractograms indicates that first growing stages (3 nm) promote polycrystalline α-W and β-W grain growth, while a few α-W$\langle 110\rangle$ oriented grains or any of these crystallographic structure combinations (nanodiffractograms 1, 10, and 17) are observed.

Up to 30 nm from the interface, β-W$\langle 100\rangle$ oriented grains and a few α-W$\langle 110\rangle$ oriented ones are observed (nanodiffractograms 3, 12, and 19). Major fiber texture components develop approximately from 30 nm above the film-substrate interface up to the free surface (nanodiffractograms 7, 15, and 22). The misorientations of α-W$\langle 110\rangle$ and α-W$\langle 111\rangle$ fiber texture axis with respect to the film-substrate interface normal are about 4° and 2°, respectively, whereas their mosaicity are ±8° and ±3°, respectively. These values are in good agreement with XRD measurements since the FWHM of the α-W{110} rocking-curve is ±8°. Grain size varies between 2 and 15 nm along the normal to the surface which is in agreement with the period determined by XRR analysis (11.0 nm). Analysis of inter-reticular distance of textured planes from nanodiffractograms revealed a compressive stress state (inter-reticular distance lower than stress-free value) and a strong stress gradient within grains (elongated spot shape), notably close to W–Cu interfaces. Some zones out of contrast are found to be α-W$\langle 111\rangle$ oriented, a result expected from our previous remarks on the relative intensities of α-W{110} and α-W{111} grains in DF-TEM images.

IV. DISCUSSION

Preferential crystallographic orientation developed during PVD is expected to be $\langle 110\rangle$ for bcc materials. This crystallographic orientation development during thin-film growth has been related to surface energy minimization.[59–62] The energy values reported in Ref. 59 are 2.9975 J/m^2 and 3.6713 J/m^2 for (110) and (111) planes, respectively. In the present study, the bcc-tungsten matrix in stratified W/Cu samples showed the expected $\langle 110\rangle$ texture for W/Cu 3/1 sample. However, samples with Cu sublayer thickness below 0.6 nm threshold showed an unexpected α-W$\langle 111\rangle$ fiber tex-

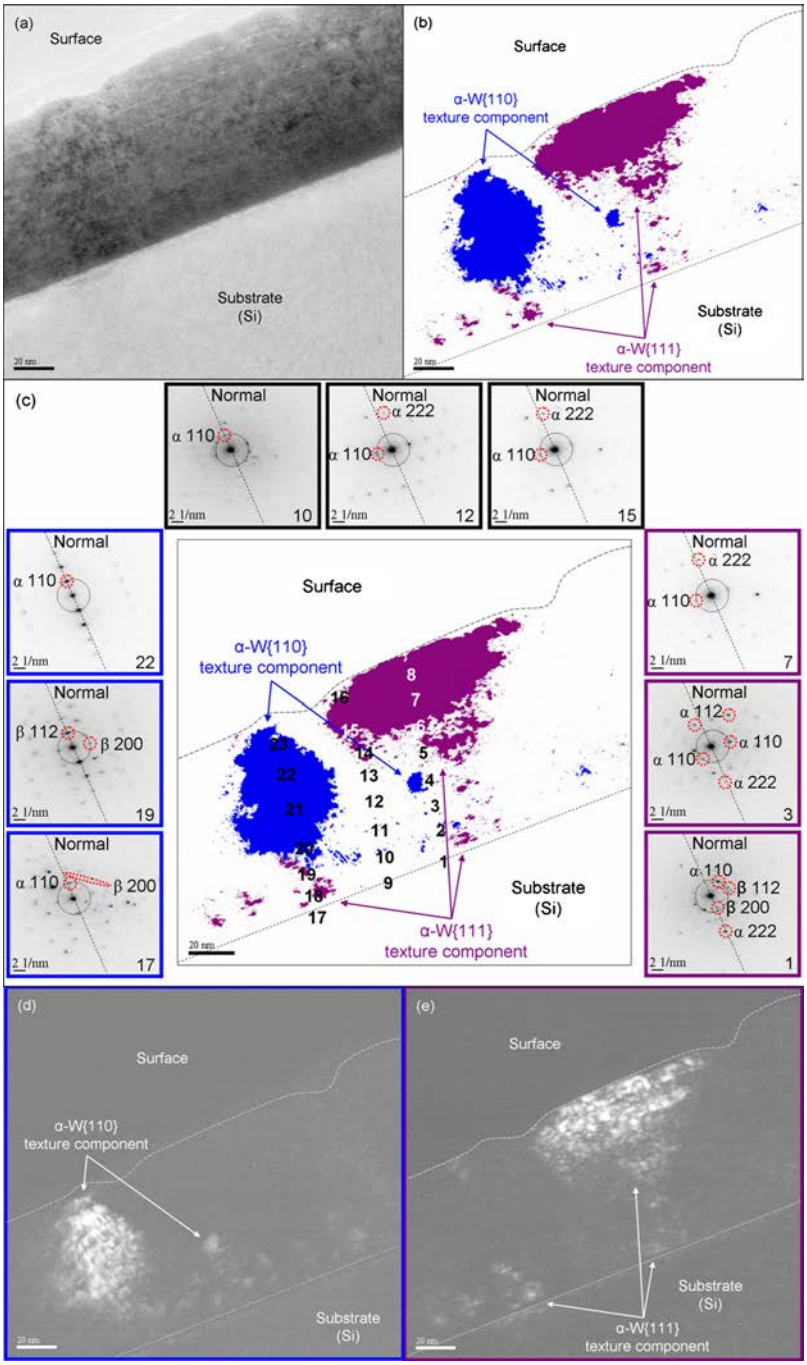

FIG. 7. (Color online) (a) BF-TEM image of W/Cu 12/0.5 specimen and (b) DF-TEM superposition: Darken regions correspond to contrasted areas observed on DF-TEM images, selecting α-W$\langle 110\rangle$ and α-W$\langle 222\rangle$ spots along the growing direction. (c) DF-TEM superposition with nanodiffraction position and typical diffraction diagrams obtained in α-W$\langle 110\rangle$, α-W$\langle 111\rangle$, and polycrystalline preferentially oriented regions. (d) and (e) are the original DF-TEM images of α-W$\langle 110\rangle$ and α-W$\langle 111\rangle$ texture components, respectively.

ture component for a bcc material (Table I) that cannot be explained apparently by surface energy minimization only.

Wei *et al.*[63] have already reported {110} and {111} fiber texture components in 700 nm fcc copper thin films deposited by magnetron sputtering while it is expected to be {111} only. The double texture was then explained by a compromise between surface energy and volume elastic energy which are both *hkl* dependent because of copper elastic anisotropy,[64] an effect which cannot be involved in the present case since tungsten is elastically isotropic.

XRR (Fig. 5) and GISAXS (Fig. 6) revealed that all stratified W/Cu samples present an original structure with copper nanoparticles dispersed in a tungsten matrix. Dispersion is characterized by an in-plane homogeneous particle distribution (associated to a copper Volmer–Weber growth)[65] differing from the inter-particle distance along the normal to the thin-film surface (controlled by the sputtering sequence). Previous studies report that under layer roughness may influence the development of layers crystallographic orientation,[66,67] as the substrate does.[68] Samples with 0.2 nm copper thickness and sequenced tungsten deposition do present the α-W$\langle 111\rangle$ fiber texture component. However, above a Cu concentration threshold of 0.6 nm, the α-W$\langle 111\rangle$ fiber texture component is lost (Figs. 4 and 5). Yet, GISAXS measurements revealed copper sublayer discontinuities in both W/Cu 3/0.5 and W/Cu 3/1 and thus let suppose minor impact of the roughness induced by dispersed copper inclusions. TEM observations confirmed that both substrate and interfaces were not affecting significantly the crystallo-

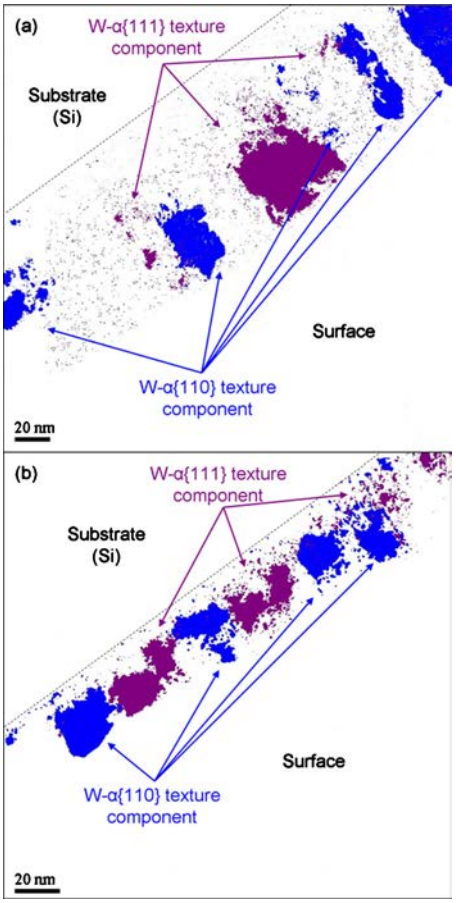

FIG. 8. (Color online) DF-TEM superposition of two different zones of W/Cu 12/0.5 specimen. Darken regions correspond to contrasted areas observed on DF-TEM images selecting α-W⟨110⟩ and α-W⟨222⟩ texture component spots.

graphic orientation since α-W⟨110⟩, α-W⟨111⟩, and polycrystalline regions were observed regardless of the crystalline structure (i.e., phase and crystallographic orientation) in the early stages of growth (Fig. 7). Roughness induced by copper nanoparticle dispersion is thus not involved in the occurrence of the α-W⟨111⟩ fiber texture component. Moreover, nanodiffraction analysis [Fig. 7(c)] showed that main preferential crystallographic orientations develop on either α-W or β-W grains. This observation excludes *de facto* any fundamental influence of β-W and is confirmed by the presence of the α-W⟨111⟩ fiber texture component in both W/Cu 3/0.5 (which contains no β-W phase) and W/Cu 3/0 (where a large β-W phase proportion was detected).

Intragranular macroscopic residual stresses analysis (Table I) revealed significantly lower residual stress (1 GPa) for the samples without α-W⟨111⟩ fiber texture component. Hence, residual stress relaxation seems to be correlated with the loss of α-W⟨111⟩ preferential crystallographic orientation. Ganne *et al.*[69] associated the α-W⟨111⟩ fiber texture development to residual stress decrease with increasing film thickness. Indeed, Dobrev[70] proposed an explanation in terms of energetic atomic processes for fiber texture development in relation with crystalline lattice ionic channeling. During an impact between an energetic incident particle and a deposited crystalline network, energy is dissipated by partial recrystallization related to either material local fusion (thermal spike) or defect formation resulting from atom collisions. As a consequence, incident particle energy is absorbed in a volume that increases with incident atoms channeling capability that depends on the growing grains crystallographic orientation. Crystals that undergo low atomic rearrangements serve as nucleation sites for recrystallization of less favorably oriented grains deeply affected by irradiation. These channeling directions are crystallographic directions of high atomic density planes. For bcc materials, channeling increases according to the following orientation sequence ⟨110⟩, ⟨100⟩, and ⟨111⟩, the latter being the most efficient. Moreover, according to Thornton and Hoffman,[71] under energetic deposition conditions, a dense structure and compressive stresses build up. Growth of α-W⟨111⟩ crystallographic orientation is supposed to yield the lowest defects density and thus the lowest intrinsic residual stress in the opposite trend to our observations excepted for sample W/Cu 1.5/0.5 where the level of residual stress in grains with α-W⟨111⟩ texture is substantially less than in grains with other α-W⟨110⟩ texture. This last trend could be explained by W(Cu) solid solution formation which is a predominant effect for this sample.

It is thus possible that other parameters such as surface stresses or strains and as detailed below solid solution formation for low copper coverage participate to fiber texture component development.[72] Recently, Pao *et al.*[73] have shown by atomistic simulation that surface adatoms either reduce or increase surface stress depending on the copper surface orientation. Beyond coverage of 25% (as for our experimental values obtained for 0.2 and 0.6 nm thicknesses—see Sec. III A), the surface stress increases but returns to that of the singular surface as the coverage approaches a full monolayer. However, our experimental case is much more complex since chemical effects at interfaces may appear and could also considerably modify surface energies. Indeed, alloys can be obtained by PVD at interfaces between immiscible materials (at equilibrium).[74,75] In stratified thin films, Ouyang *et al.* obtained by molecular dynamic simulation an increase in copper atomic diffusion coefficient in tungsten sublayer as thickness, i.e., grain size decreases,[35,76] greatly enhancing the system solubility.[77] This phenomenon was confirmed experimentally by Villain *et al.*[37] on W/Cu multilayers. Changes in tungsten surfaces state[78] lead to interfacial energy modification between tungsten and copper.[61] This interfacial "melting" leads to a modification of interatomic interaction with changes in the nature of first neighbors of both tungsten and copper atoms. Copper diffusion is particularly enhanced in the case of PVD since this process induces energetic deposited atoms leading to ballistic effects and high atomic mobility. This effect is emphasized as the density of interfaces increases (sublayer thickness decrease, low copper coverage) and thus affects fiber texture development.

A solid solution is evidenced for 0.2 nm copper thickness since the lowest stress-free lattice parameter is reached for the 3 nm W thickness series. This phenomenon does not happen above 0.6 nm Cu thickness threshold since the stress-free lattice parameter is larger than the bulk one. In that case, we suggest that copper adsorption on tungsten surfaces hap-

pens. The important change in terms of copper coverage (adsorption versus diffusion) is determinant for the understanding of the observed behavior since the surface energy anisotropy increases with copper adsorption.[79] We suggest that the abrupt change in W texture is ruled by this phenomenon. Below a copper thickness threshold of 0.6 nm, a fiber texture mixture is obtained as for a tungsten surface since copper diffuses into the tungsten layer. Only above this threshold the copper is in sufficient quantity to impede the ⟨111⟩ fiber texture formation.

V. CONCLUSION

Complementary techniques were used in order to characterize PVD W/Cu multilayer stratification and texture development, both uncommon. GISAXS, XRR, and TEM measurements showed that copper atoms arrange in nanoparticles which are homogeneously dispersed in sublayer due to a Volmer–Weber growth and periodically spaced in the tungsten matrix by the sputtering sequence. Major preferential crystallographic orientation of α-W matrix evolved from a single ⟨110⟩ fiber texture component (usually encountered in bcc materials deposited by PVD) to a combination of ⟨110⟩ and ⟨111⟩ fiber texture components below a 0.6 nm threshold of copper thickness, whereas an important polycrystalline volume fraction remains present. DF-TEM images were used to determine the relative arrangements of α-W⟨110⟩ or α-W⟨111⟩ oriented crystalline zones; no clear correlation between crystalline growth and W–Cu interfaces has been evidenced. In addition, electron nanodiffraction supplied detailed features at local scale of crystallographic structure development. DF-TEM analysis revealed a columnar growth of both fiber texture components that starts simultaneously at 30 nm from the film-substrate interface. Nanodiffractograms analysis indicated that the initial layer (first 30 nm) is composed of polycrystalline grains (which are mainly composed of α-W phase with a few amount of β-W phase). The results clearly showed that the presence of β-W phase does not influence the fiber texture development of α-W. For copper thickness larger than 0.6 nm, the α-W matrix both exhibits random distribution of grains associated with a strong ⟨110⟩ fiber texture component. This ⟨110⟩ fiber texture components is expected for PVD processes (surface energy minimization in bcc materials). For copper thickness below the 0.6 nm threshold (coverage of 63%), α-W matrix exhibits two major fiber texture components, namely ⟨110⟩ and ⟨111⟩ ones (still associated with an important polycrystalline volume fraction). These microstructure changes have to be interpreted in view of the formation of a solid solution evidenced for 0.2 nm copper thickness whereas above 0.6 nm Cu thickness copper adsorption on tungsten surfaces happens. This scenario (diffusion versus adsorption) explained the abrupt change in W fiber texture.

In this paper, we were interested in producing reference microstructures for mechanical testing.[80] One important point to consider for achieving microstructural tailoring is that texture component development must be controlled. Our results show that adding copper thickness in a multilayer structure allows tailoring the microstructure: grain size is about the thickness of the layer (for size effect studies) and above a threshold copper thickness, one texture component is selected from the initial two texture components. In addition, the mechanical state in the film is simplified and the magnitude of the stresses is reduced by a factor 2. A recent paper from Vodnick *et al.*[81] has shown the complexity of the mechanical state when strong texture components are present.

ACKNOWLEDGMENTS

The authors would like to acknowledge Dr. Philippe Guérin for stimulating discussions and technical support with coating depositions and the D2AM ESRF beam-line team for technical assistance during GISAXS measurements.

[1] H. Gleiter, Acta Mater. **48**, 1 (2000).
[2] H. Gleiter, in *Deformation of Polycrystals: Mechanisms and Microstructures*, edited by N. Hansen, A. Horsewell, T. Leffers, and H. Lilholt (Risø National Laboratory, Roskilde, Denmark, 1981), pp. 15–21.
[3] H. Gleiter, Nanostruct. Mater. **6**, 3 (1995).
[4] W. D. Nix, Metall. Trans. A **20**, 2217 (1989).
[5] R. P. Vinci and J. J. Vlassak, Annu. Rev. Mater. Sci. **26**, 431 (1996).
[6] J. Schiøtz, T. Vegge, F. D. Di Tolla, and K. W. Jacobsen, Phys. Rev. B **60**, 11971 (1999).
[7] S. Yip, Nature (London) **391**, 532 (1998).
[8] H. Van Swygenhoven and J. R. Weertman, Mater. Today **9**, 24 (2006).
[9] S. Cuenot, C. Frétigny, S. Demoustier-Champagne, and B. Nysten, Phys. Rev. B **69**, 1 (2004).
[10] F. Spaepen and D. Y. W. Yu, Scr. Mater. **50**, 729 (2004).
[11] E. Arzt, Acta Mater. **46**, 5611 (1998).
[12] M. A. Meyers, A. Mishra, and D. J. Benson, Prog. Mater. Sci. **51**, 427 (2006).
[13] S. Yoo, M. S. Krupashankara, T. S. Sudarshan, and R. J. Dowding, Mater. Sci. Technol. **14**, 170 (1998).
[14] A. Luedtke, Adv. Eng. Mater. **6**, 142 (2004).
[15] K. V. Sebastian, Int. J. Powder Metall. & Powder Technol. **17**, 297 (1981).
[16] M. Gasik, Comput. Mater. Sci. **13**, 42 (1998).
[17] Y. J. Lee, B. H. Lee, G. S. Kim, D. G. Kim, D. S. Kim, and Y. D. Kim, Mater. Lett. **60**, 2000 (2006).
[18] P. M. Geffroy, T. Chartier, and J. F. Silvain, Adv. Eng. Mater. **9**, 547 (2007).
[19] D. J. Ilic, J. Fiscina, C. G. Oliver, N. Ilicacute, and F. Mücklich, Adv. Eng. Mater. **9**, 542 (2007).
[20] B. L. Mordike, J. Kaczmar, M. Kielbinski, and K. U. Kainer, Powder Metall. **23**, 91 (1991).
[21] A. Neubrand and J. Rödel, Z. Metallkd. **88**, 358 (1997).
[22] Y. D. Kim, N. L. Oh, S. T. Oh, and I. H. Moon, Mater. Lett. **51**, 420 (2001).
[23] A. Mortensen and S. Suresh, Int. Mater. Rev. **40**, 239 (1995).
[24] I. H. Moon and J. S. Lee, Powder Metall. **22**, 5 (1979).
[25] J. C. Kim, S. S. Ryu, Y. D. Kim, and I. H. Moon, Scr. Mater. **39**, 669 (1998).
[26] R. Jedamzik, A. Neubrand, and J. Rodel, J. Mater. Sci. **35**, 477 (2000).
[27] M. Gupta and C. Y. Loke, Mater. Sci. Eng., A **276**, 210 (2000).
[28] G. Gusmano, A. Bianco, R. Polini, P. Magistris, and G. Marcheselli, J. Mater. Sci. **36**, 901 (2001).
[29] S. B. Li and J. X. Xie, Compos. Sci. Technol. **66**, 2329 (2006).
[30] X. L. Shi, H. Yang, G. Q. Shao, X. L. Duan, L. Yan, Z. Xiong, and P. Sun, Mater. Sci. Eng., A **457**, 18 (2007).
[31] J. C. Y. Koh and A. Fortini, Int. J. Heat Mass Transfer **16**, 2013 (1973).
[32] Y. G. Chen and B. X. Liu, J. Phys. D **30**, 1729 (1997).
[33] W. Hiller, M. Buchgeister, P. Eitner, K. Kopitzki, V. Lillienthal, and E. Peiner, Mater. Sci. Eng., A **115**, 151 (1989).
[34] J. A. Thornton and J. E. Greene, in *Handbook of Deposition Technologies for Films and Coatings*, 2nd ed., edited by R. F. Bunshah (Noyes, Park Ridge, NJ, 1994).
[35] G. Ouyang, C. X. Wang, and G. W. Yang, Appl. Phys. Lett. **86**, 1 (2005).
[36] P. Goudeau, P. Villain, T. Girardeau, P. O. Renault, and K. F. Badawi, Scr. Mater. **50**, 723 (2004).
[37] P. Villain, P. Goudeau, K. F. Badawi, G. Ouyang, G. W. Yang, and V. Pélosin, J. Mater. Sci. **42**, 7446 (2007).

[38]O. Castelnau, G. Geandier, P.-O. Renault, Ph. Goudeau, and E. Le Bourhis, Thin Solid Films **516**, 320 (2007).
[39]I. C. Noyan and J. B. Cohen, *Residual Stress Measurement by Diffraction and Interpretation* (Springer, New York, 1987).
[40]V. Hauk, *Structural and Residual Stress Analysis by Non Destructive Methods: Evaluation, Application, Assessment* (Elsevier, Amsterdam, 1997).
[41]B. Girault, V. Vidal, L. Thilly, P.-O. Renault, P. Goudeau, E. Le Bourhis, P. Villain-Valat, G. Geandier, J. Tranchant, J.-P. Landesman, P.-Y. Tessier, B. Angleraud, M.-P. Besland, A. Djouadi, and F. Lecouturier, Int. J. Nanotechnol. **5**, 609 (2008).
[42]D. Babonneau, J. Appl. Crystallogr. **43**, 929 (2010).
[43]I. A. Weerasekera, S. l. Shah, D. V. Baxter, and K. M. Unruh, Appl. Phys. Lett. **64**, 3231 (1994).
[44]Y. G. Shen and Y. W. Mai, J. Mater. Sci. **36**, 93 (2001).
[45]P. Villain, P. Goudeau, J. Ligot, S. Benayoun, K. F. Badawi, and J.-J. Hantzpergue, J. Vac. Sci. Technol. A **21**, 967 (2003).
[46]K. Pawlik and P. Ozga, Göttinger Arbeiten zur Geologie und Paläontologie SB4 (1999).
[47]K. Pawlik, Mater. Sci. Forum **133–136**, 151 (1993).
[48]R. O. Williams, J. Appl. Phys. **39**, 4329 (1968).
[49]J. Imhof, Textures Microstruct. **4**, 189 (1982).
[50]S. Matthies and G. W. Vinel, Phys. Status Solidi B **112**, K111 (1982).
[51]P. Villain, Ph.D. thesis, Poitiers University, 2002.
[52]J. M. Cowley and J. C. H. Spence, in *Handbook of Nanostructured Materials and Nanotechnology*, edited by H. S. Nalwa (Academic, San Diego, 2000), Vol. 2, pp. 1–87.
[53]D. Babonneau, G. Abadias, J. Toudert, T. Girardeau, E. Fonda, J. S. Micha, and F. Petroff, J. Phys.: Condens. Matter **20**, 035218 (2008).
[54]N. Durand, K. F. Badawi, and P. Goudeau, J. Appl. Phys. **80**, 5021 (1996).
[55]Y. Adda, J. M. Dupouy, J. Philibert, and Y. Quéré, *Eléments de Métallurgie Physique* (INSTN–CEA, Saclay, France, 1987).
[56]P. Beauchamp, R. Taylor, and V. Vitek, J. Phys. F: Met. Phys. **5**, 2017 (1975).
[57]D. L. Davidson and F. R. Brotzen, J. Appl. Phys. **39**, 5768 (1968).
[58]P. Olsson, I. A. Abrikosov, L. Vitos, and J. Wallenius, J. Nucl. Mater. **321**, 84 (2003).
[59]S. G. Wang, E. K. Tian, and C. W. Lung, J. Phys. Chem. Solids **61**, 1295 (2000).
[60]Y. Gotoh, S. Entani, and H. Kawanowa, Surf. Sci. **507–510**, 401 (2002).
[61]G. Ouyang, L. H. Liang, C. X. Wang, and G. W. Yang, Appl. Phys. Lett. **88**, 091914 (2006).
[62]J. M. Zhang, D. D. Wang, and K. W. Xu, Appl. Surf. Sci. **252**, 8217 (2006).
[63]H. L. Wei, H. Huanga, C. H. Woo, R. K. Zheng, G. H. Wen, and X. X. Zhang, Appl. Phys. Lett. **80**, 2290 (2002).
[64]J. M. Zhang, Y. Zhang, and K. W. Xu, J. Cryst. Growth **285**, 427 (2005).
[65]C. V. Thompson, Annu. Rev. Mater. Sci. **30**, 159 (2000).
[66]C. E. Murray, K. P. Rodbell, and P. M. Vereecken, Thin Solid Films **503**, 207 (2006).
[67]N. R. Shamsutdinov, A. J. Böttger, and F. D. Tichelaar, Scr. Mater. **54**, 1727 (2006).
[68]R. Hoogeveen, M. Moske, H. Geisler, and K. Samwer, Thin Solid Films **275**, 203 (1996).
[69]T. Ganne, J. Crépin, S. Serror, and A. Zaoui, Acta Mater. **50**, 4149 (2002).
[70]D. Dobrev, Thin Solid Films **92**, 41 (1982).
[71]J. A. Thornton and D. W. Hoffman, Thin Solid Films **171**, 5 (1989).
[72]L. H. He, C. W. Lim, and B. S. Wu, Int. J. Solids Struct. **41**, 847 (2004).
[73]C.-W. Pao, D. J. Srolovitz, and C. V. Thompson, Phys. Rev. B **74**, 155437 (2006).
[74]E. Ma, Prog. Mater. Sci. **50**, 413 (2005).
[75]J. C. Kim, S. S. Ryu, H. Lee, and I. H. Moon, Int. J. Powder Metall. **35**, 7 (1999), (Princeton, NJ).
[76]G. Ouyang, C. X. Wang, S. W. Li, X. Zhou, and G. W. Yang, Appl. Surf. Sci. **252**, 3993 (2006).
[77]G. Ouyang, X. Tan, C. X. Wang, and G. W. Yang, Nanotechnology **17**, 4257 (2006).
[78]X. K. Shu, P. Jiang, and J. G. Che, Surf. Sci. **545**, 199 (2003).
[79]S. P. Chen, Surf. Sci. Lett. **274**, L619 (1992).
[80]G. Geandier, D. Thiaudiere, R. N. Randriamazaoro, R. Chiron, S. Djaziri, B. Lamongie, Y. Diot, E. Le Bourhis, P.-O. Renault, P. Goudeau, A. Bouaffad, O. Castelnau, D. Faurie, and F. Hild, Rev. Sci. Instrum. **81**, 103903 (2010).
[81]A. M. Vodnick, D. E. Nowak, S. Labat, O. Thomas, and S. P. Baker, Acta Mater. **58**, 2452 (2010).